

High CO depletion in southern infrared-dark clouds

F. Fontani^{1*}, A. Giannetti², M.T. Beltrán¹, R. Dodson³, M. Rioja³, J. Brand²
P. Caselli⁴ and R. Cesaroni¹

¹ *INAF-Osservatorio Astrofisico di Arcetri, L.go E. Fermi 5, Firenze, I-50125, Italy*

² *INAF-Istituto di Radioastronomia, via P. Gobetti 101, Bologna, I-40129, Italy*

³ *International Centre for Radio Astronomy Research, University of Western Australia, Perth, Australia*

⁴ *School of Physics and Astronomy, University of Leeds, Leeds, LS2 9JT, UK*

Accepted date. Received date; in original form date

ABSTRACT

Infrared-dark high-mass clumps are among the most promising objects to study the initial conditions of the formation process of high-mass stars and rich stellar clusters. In this work, we have observed the (3–2) rotational transition of C^{18}O with the APEX telescope, and the (1,1) and (2,2) inversion transitions of NH_3 with the Australia Telescope Compact Array in 21 infrared-dark clouds already mapped in the 1.2 mm continuum, with the aim of measuring basic chemical and physical parameters such as the CO depletion factor (f_{D}), the gas kinetic temperature and the gas mass. In particular, the C^{18}O (3–2) line allows us to derive f_{D} in gas at densities higher (and hence potentially more depleted) than that traced by the (1–0) and (2–1) lines, typically used in previous works. We have detected NH_3 and C^{18}O in all targets. The clumps have a median mass of $\sim 244 M_{\odot}$, are gravitationally bound, have an average kinetic temperature of 17 K and possess mass, H_2 column and surface densities consistent with being potentially the birthplace of high-mass stars. We have measured f_{D} in between 5 and 78, with a mean value of 32 and a median of 29. These values are, to our knowledge, larger than the typical CO depletion factors measured towards infrared-dark clouds and high-mass dense cores, and are comparable to or larger than the values measured in low-mass pre-stellar cores close to the onset of the gravitational collapse. This result suggests that the earliest phases of the high-mass star and stellar cluster formation process are characterised by f_{D} larger than in low-mass pre-stellar cores. On the other hand, f_{D} does not seem to be correlated to any other physical parameter, except for a faint anti-correlation with the gas kinetic temperature. Thirteen out of 21 clumps are undetected in the 24 μm Spitzer images, and have slightly lower kinetic temperatures, masses and H_2 column densities with respect to the eight Spitzer-bright sources. This could indicate that the Spitzer-dark clumps are either less evolved or are going to form less massive objects.

Key words: Molecular data – Stars: formation – radio lines: ISM – submillimetre: ISM – ISM: molecules

1 INTRODUCTION

An ever increasing number of observational evidences indicates that the earliest phases of massive star and stellar cluster formation occur within infrared dark clouds (IRDCs). These are dense molecular clouds seen as extinction features against the bright mid-infrared Galactic background (e.g. Simon et al 2006, Ragan et al. 2006, 2011, Rathborne et al. 2007, 2010, Butler & Tan 2009). IRDCs are characterised by very high gas column densities ($10^{23} - 10^{25} \text{cm}^{-2}$)

and low temperatures ($\leq 25 \text{ K}$), so that they are believed to be the place where most of the stars in our Galaxy are being formed.

From an observational point of view, the spatial distribution of the IRDCs in the Galaxy follows that of the molecular galactic component (with a concentration in the so-called 5 kpc molecular ring), and they are strong emitters of both far-IR/millimetre continuum and rotational molecular transitions, especially those characterised by a high critical density. In many of them, observations of the dense gas at sub-parsec linear scales revealed the presence of ongoing star formation, both in isolated and clustered mode

* E-mail: fontani@arcetri.astro.it

(e.g. Beuther & Sridharan 2007, Zhang et al. 2009, Fontani et al. 2009, Jiménez-Serra et al. 2010, Pillai et al. 2011), including clear signs of high-mass star formation like hot cores (e.g. Rathborne et al. 2008) and/or Ultracompact HII regions (Battersby et al. 2010). This demonstrates that IRDCs are indeed the birthplace of stars and stellar clusters of all masses. Therefore, the IRDCs in the earliest evolutionary stages are the best locations where to study the initial conditions of the star formation process and put constraints on current theories.

Despite the identification of thousands of IRDCs, the number of studies devoted to unveiling their physical and chemical properties remains still limited. There are very few targeted studies, especially in the southern hemisphere (e.g. Vasyunina et al. 2009, Miettinen et al. 2011), where there are fewer groundbased facilities operating in the (sub-)millimetre and centimetre domain than there are in the north. In particular, very little is known about the chemistry of IRDCs: studies suggest chemical compositions similar to those observed in low-mass pre-stellar cores (Vasyunina et al. 2009), including large abundances of deuterated species (Pillai et al. 2007; Pillai et al. 2011; Fontani et al. 2011). However, the amount of CO freeze-out, a key chemical parameter for pre-stellar cores (see e.g. Bergin & Tafalla 2007 for a review) remains controversial: some works indicate high levels (factor of 5, Hernández et al. 2011) of CO freeze-out, while others do not reveal significant CO depletion (e.g. Miettinen et al. 2011).

In this work we present observations of the rotational transition (3–2) of the dense gas tracer C^{18}O , performed with the Atacama Pathfinder EXperiment (APEX) 12-m Telescope, and of the inversion transitions (1,1) and (2,2) of NH_3 carried out with the Australia Telescope Compact Array (ATCA), towards 21 IRDCs with declination lower than -30° already mapped in the 1.2 mm continuum. The C^{18}O observations allow to compute the CO depletion factor, while the ammonia inversion transitions can be used to derive the temperature in dense and cold gas (see e.g. Ho & Townes 1983). Observations of N_2H^+ and N_2D^+ in some of the target sources, useful to derive the amount of deuterated fraction (by comparing the N_2D^+ and N_2H^+ column densities), are also presented. In Sect. 2 we describe the criteria applied to select the targets. Sect. 3 gives an overview of the observations. The results are presented in Sect. 4 and discussed in Sect. 5. Conclusions and a summary of the main findings are given in Sect. 6.

2 TARGET SELECTION

We selected 21 IRDCs from the 95 massive millimetre clumps detected by Beltrán et al. (2006) in the 1.2 mm continuum and non-MSX emitters (neither diffuse nor point-like). The targets were chosen according to these criteria: (i) source declination $\delta \leq -30^\circ$; (ii) clumps isolated or having the emission peak separated by more than the SIMBA half power beam width to that of MSX-emitter objects, to limit confusion and select the most quiescent sources; (iii) clump masses above $\sim 35M_\odot$ to deal with possible massive star formation. In this work we have recomputed the masses utilising the gas temperature derived from ammonia for each clump, and our results confirm that all targets are high-mass

clumps (see Sect 4.6). The list of IRDCs is given in Table 1. The coordinates correspond to the peak of the 1.2 millimetre continuum emission mapped by Beltrán et al. (2006). In Table 1 we also give some basic information like the distance to the Sun, the Galactocentric distance, and the (non-)detection in the Spitzer-MIPS 24 μm images. A comparison between the 1.2 mm continuum maps and the Spitzer 24 μm images of each target (except for 13039–6108c6, for which the MIPS images are not available) is shown in Fig. A1 of Appendix A.

3 OBSERVATIONS

3.1 APEX

Single-point spectra of the C^{18}O (3–2), N_2H^+ (3–2) and N_2D^+ (4–3) lines towards the sources listed in Table 1 were obtained with the APEX Telescope in service mode between the 20th and the 28th of June, 2008. The observations were performed in the wobbler-switching mode with a $150''$ azimuthal throw and a chopping rate of 0.5 Hz. The receiver used for all lines was SHFI/APEX-2. The backend provided a total bandwidth of 1000 MHz. Details about the observed lines and the observational parameters are given in Table 2. The telescope pointing and focusing were checked regularly by continuum scans on planets and the corrections were applied on-line. Calibration was done by the chopper-wheel technique. Spectra were obtained in antenna temperature units (corrected for atmospheric attenuation), T_A^* , and then converted to main beam temperature units through the relation $T_{\text{MB}} = \frac{F_{\text{eff}}}{B_{\text{eff}}} T_A^*$ (F_{eff} and B_{eff} are given in Col. 5 of Table 2). The velocities adopted to centre the backends are given in Col. 6 of Table 1. For most sources we knew the radial Local Standard of Rest velocities (V_{LSR}) from previous CS observations. The spectra of 16435–4515c3 (for which we did not have the CS data) were centred at $V_{\text{LSR}} = 0$; in any case the total bandwidth of the backend ($\sim 1000 \text{ km s}^{-1}$) was larger than the velocity gradient across the Galaxy.

3.2 ATCA

We observed the inversion transitions $(J, K) = (1, 1)$ and $(2, 2)$ of ammonia at 23694.5 MHz and 23722.6 MHz (K-band at $\sim 1.2 \text{ cm}$), respectively, with the ATCA¹ towards all targets in Table 1. The observations were performed between the 4th and the 8th of March, 2011, for a total telescope time of 48 hours. We used the configuration 750D, which provides baselines between 31 and 4469 m. The primary beam was $\sim 2.5'$ at the line frequencies. The flux density scale was established by observing the standard primary calibrator 1934–638, and the uncertainty is expected to be of the order of $\sim 10\%$. Gain calibration was ensured by frequent observations of nearby compact quasars. The quasar 0537–441 was used for passband calibration. Pointing corrections were derived from nearby quasars and applied online. Atmospheric conditions were generally good (weather path noise $\simeq 400 \mu\text{m}$ or better).

¹ The Australia Telescope Compact Array is part of the Australia Telescope which is funded by the Commonwealth of Australia for operation as a National Facility managed by CSIRO.

Table 1. Source list and detection summary.

Source name ^a	R.A. (J2000) h m s	Dec. (J2000) ° ' "	l °	b °	V_{LSR}^b km s ⁻¹	d^c kpc	D_{GC} kpc	MIPS 24 μm^d
08477–4359c1	08:49:35.13	–44:11:59	264.69	–0.07	8.5	1.8	8.9	Y
13039–6108c6	13:07:14.80	–61:22:55	305.18	1.14	–26.2	2.4	7.4	–
13560–6133c2	13:59:33.04	–61:49:13	311.23	–0.35	–58.4	5.6	6.4	N
14183–6050c3	14:22:21.54	–61:06:42	314.03	–0.52	–42.6	3.4	6.6	N
15038–5828c1	15:07:32.52	–58:40:33	320.19	–0.77	–67.1	5.0	5.7	N
15278–5620c2	15:31:44.17	–56:32:08	324.07	–0.73	–49.4	3.4	6.1	N
15470–5419c1	15:51:28.24	–54:31:42	327.51	–0.83	–61.7	4.1	5.5	Y ^e
15470–5419c3	15:51:01.62	–54:26:46	327.51	–0.72	–61.7	4.1	5.5	Y
15557–5215c2	15:59:36.20	–52:22:58	329.81	0.03	–67.6	4.4	5.2	Y
15557–5215c3	15:59:39.70	–52:25:14	329.80	–0.00	–67.6	4.4	5.2	N ^f
16061–5048c1	16:10:06.61	–50:50:29	332.06	0.08	–51.8	3.6	5.6	Y
16061–5048c4	16:10:06.61	–50:57:09	331.98	0.00	–51.8	3.6	5.6	N ^f
16093–5128c2	16:12:55.46	–51:43:22	331.77	–0.86	–97.3	6.1	4.3	N
16093–5128c8	16:12:49.63	–51:36:34	331.84	–0.77	–97.3	6.1	4.3	N ^g
16164–4929c3	16:20:24.51	–49:35:34	334.11	–0.17	–33.8	2.6	6.3	N ^g
16254–4844c1	16:29:00.89	–48:50:31	335.63	–0.65	–45.5	3.4	5.6	Y
16435–4515c3	16:47:33.13	–45:22:51	340.31	–0.71	0.0	– ^h	4.9	N
16482–4443c2	16:51:44.59	–44:46:50	341.24	–0.90	–43.3	3.7	5.1	N ^f
16573–4214c2	17:00:33.38	–42:25:18	344.08	–0.67	–23.7	2.6	6.0	Y
17040–3959c1	17:07:58.78	–40:02:24	346.82	–0.35	–0.4	16.5 ⁱ	8.5	N? ^l
17195–3811c2	17:23:00.30	–38:14:58	349.97	–1.68	–26.4	3.6	5.0	Y

^a derived from the IRAS source name and the 'clump' number assigned by Beltrán et al (2006);^b from the CS (2–1) or (3–2) transitions (Fontani et al. 2005);^c kinematic distance from the Sun (Beltrán et al 2006). In case of distance ambiguity, the near distance is adopted;^d detection (Y) or non-detection (N) of the clump in the Spitzer-MIPS 24 μm band;^e point-like infrared source not at clump centre, probably associated with it;^f point-like infrared source at the edge of the 3 σ rms contour level of the millimetre continuum, probably not associated with it;^g diffuse infrared emission inside the 3 σ rms contour level of the millimetre continuum, probably associated with a nearby infrared object;^h the kinematic distance recomputed in Sect. 4.6 from the C¹⁸O (3–2) line peak velocity is 3.1 kpc;ⁱ near distance smaller than 100 pc, so that the far distance is adopted;^l the millimetre map of the clump is incomplete because at the edge of the SIMBA field of view, thus one cannot conclusively assert if the clump is associated with an infrared source (see Fig. A1).**Table 2.** Transitions observed with APEX and observational parameters.

Transition	ν^a GHz	HPBW "	ΔV^b km s ⁻¹	$B_{\text{eff}}/F_{\text{eff}}$	T_{sys} K
C ¹⁸ O (3–2)	329.331	18.9	~ 0.22	0.74/0.95	200 – 300 ^c
N ₂ D ⁺ (4–3)	308.422 ^d	20.2	~ 0.23	0.74/0.95	160 – 300
N ₂ H ⁺ (3–2)	279.512 ^e	22.3	~ 0.26	0.74/0.95	130 – 160

^a line rest frequency;^b spectral resolution;^c for 13039–6108c6, 13560–6133c2 and 14183–6050c3, $T_{\text{sys}} \sim 600$ K;^d from the Cologne Database for Molecular Spectroscopy (CDMS), and it refers to the $F_1 F = 5\ 5 \rightarrow 4\ 4$ hyperfine component;^e from Pagani et al. (2009), and it refers to the $F_1 F = 4\ 5 \rightarrow 3\ 4$ hyperfine component, which has a relative intensity of 17.46%.

The total time was broken up into series of 3-/5-minute snapshots in order to improve the coverage of the uv-plane for each target. As a consequence of this observing strategy, the integration time on source is variable, and generally in between ~ 30 mins and ~ 1 hour. The CABB² correlator provided two "zoom" bands of 64 MHz each, with a spec-

tral resolution in each zoom of 32 kHz (~ 0.4 km s⁻¹ at the frequencies of the lines). The ammonia lines were observed in one zoom band. The data were edited and calibrated following standard tasks and procedures of the MIRIAD software package. After the editing and calibration in MIRIAD, the data were imported in AIPS. Imaging and deconvolution were performed using the 'imagr' task, applying natural weighting to the visibilities. The ammonia emission was detected only on the short baselines, thus we discarded all

² <http://www.narrabri.atnf.csiro.au/observing/CABB.html>

baselines $> 30 \text{ k}\lambda$. In order to obtain images with the same angular resolution, and comparable to the APEX beam, we reconstructed the images with a circular beam of $20''$ of diameter for all sources, except for 17195-3811c2 and 17040-3959c1, that have a poorer UV-coverage, and for which we get a beam of roughly $20'' \times 40''$. Moreover, 16254-4844c1 and 16573-4214c2 were observed only once, making the clean impossible and thus forcing us to use the dirty image deconvolved with the dirty beam to determine the spectrum.

In this work the ATCA data will be used only to derive the gas temperature from the NH_3 (1,1) and (2,2) spectra at the dust emission peak (in Sect. 4.5). A complete presentation and analysis of the ATCA observations will be given in a forthcoming paper (Giannetti et al., in prep).

4 RESULTS

4.1 Detection summary

The detection summary is given in Table 3. C^{18}O (3-2) was observed and detected in all sources. Twelve targets were also observed and detected in N_2H^+ (3-2). Ten clumps were observed in N_2D^+ (4-3), and only clump 15557-5215c2 was marginally detected. This is, to our knowledge, the first detection of this line towards an IRDC. All targets were observed and detected in the ammonia inversion transitions, with the exception of 14183-6050c3 which was undetected in the (2,2) line.

4.2 Line profiles and parameters

All spectra of the C^{18}O and N_2H^+ lines are shown in Appendix B. Fig. B1 shows the N_2H^+ (3-2) and C^{18}O (3-2) transitions in the twelve clumps observed and detected in both lines. Fig. B2 shows the nine sources observed and detected in C^{18}O (3-2) only.

Most of the C^{18}O lines are well fitted by single Gaussians. The results of these fits are reported in Table 4. Slightly asymmetric profiles deviating from the Gaussian shape can be noted in 15470-5419c1, 16061-5048c1, 16482-4443c2, 16573-4214c2 and 17040-3959c1. This could be due either to the superposition of multiple blended velocity components, or to high optical depth effects. Non-Gaussian wings in one (or both) side(s) of the line indicating presence of outflows are noticeable towards two sources, 08477-4359c1 and 17195-3811c2 (see Fig. 1). Four sources show multiple lines well-separated in velocity, 14183-6050c3, 16093-5128c2, 16093-5128c8, 16435-4515c3. Because we had the previous CS observations (Fontani et al. 2005) as reference, in Table 4 we have identified the line associated with the star-forming region of our interest. The other components are almost certainly arising from clouds along the line of sight but not associated with the star-forming region, given the large separation in velocity (from ~ 20 to $\sim 40 \text{ km s}^{-1}$, see Figs. B1 and B2).

The N_2H^+ (3-2) lines roughly peak at the same position as the C^{18}O (3-2) ones and have comparable line widths. Because of the hyperfine structure present in the transition, it is not straightforward to derive conclusions on blended multiple velocity components. However, we note hints of possible secondary velocity components in all the lines that

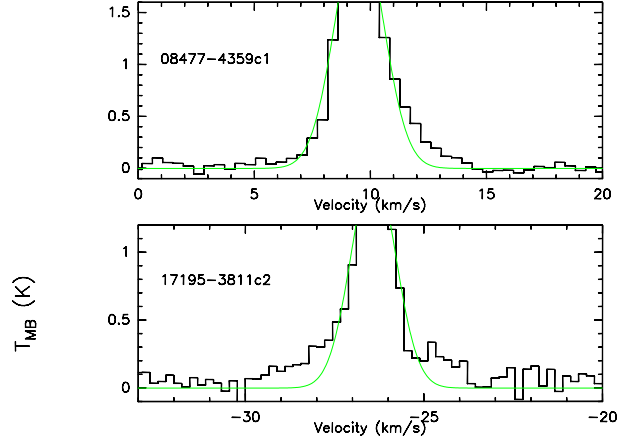


Figure 1. C^{18}O (3-2) spectra of 08477-4359c1 and 17195-3811c2. The Gaussian fits are superimposed on the spectra and highlight significant emission in non-Gaussian wings.

Table 4. C^{18}O line parameters derived from Gaussian fits. For sources with more than one velocity component, the line labelled as ‘a’ is the one associated with the IRDC (based on previous CS observations, Fontani et al. 2005).

source	$\int T_{\text{MB}} dv$ K km s $^{-1}$	v_{LSR} km s $^{-1}$	FWHM km s $^{-1}$	T_{peak} K
08477-4359c1	6.10(0.09)	9.53(0.02)	2.44(0.04)	2.3
13039-6108c6	1.4(0.1)	-26.04(0.06)	1.8(0.1)	0.76
13560-6133c2	1.6(0.15)	-57.47(0.08)	1.9(0.2)	0.8
14183-6050c3-a	0.9(0.1)	-45.52(0.08)	1.5(0.2)	0.56
14183-6050c3-b	0.57(0.06)	-26.70(0.02)	0.48(0.05)	1.1
15038-5828c1	0.9(0.1)	-69.3(0.3)	5.2(0.7)	0.16
15278-5620c2	2.5(0.1)	-49.42(0.04)	2.0(0.1)	1.18
15470-5419c1	2.3(0.1)	-58.74(0.07)	2.45(0.2)	0.88
15470-5419c3	2.6(0.1)	-61.38(0.06)	2.9(0.1)	0.84
15557-5215c2	4.2(0.1)	-67.57(0.03)	2.28(0.08)	1.7
15557-5215c3	1.7(0.1)	-68.47(0.08)	2.4(0.2)	0.67
16061-5048c1	7.61(0.02)	-67.28(0.03)	3.58(0.06)	2.0
16061-5048c4	3.2(0.1)	-51.99(0.03)	1.94(0.07)	1.6
16093-5128c2-a	3.6(0.1)	-96.19(0.05)	3.4(0.1)	1.0
16093-5128c2-b	1.97(0.07)	-63.46(0.03)	1.57(0.07)	1.2
16093-5128c8-a	0.96(0.06)	-96.85(0.08)	2.3(0.2)	0.39
16093-5128c8-b	0.19(0.04)	-68.9(0.1)	1.0(0.2)	0.18
16164-4929c3	2.95(0.07)	-33.80(0.02)	1.76(0.05)	1.6
16254-4844c1	2.72(0.09)	-44.98(0.03)	2.20(0.09)	1.2
16435-4515c3-a	1.7(0.1)	-35.57(0.04)	1.6(0.1)	1.0
16435-4515c3-b	0.88(0.09)	-52.09(0.06)	1.3(0.2)	0.62
16435-4515c3-c	0.5(0.1)	-24.4(0.1)	1.5(0.4)	0.31
16482-4443c2	4.6(0.1)	-43.35(0.05)	3.3(0.1)	1.3
16573-4214c2	8.1(0.2)	-27.29(0.03)	2.76(0.06)	2.8
17040-3959c1	6.45(0.08)	-15.87(0.02)	2.40(0.03)	2.5
17195-3811c2	2.54(0.07)	-26.41(0.02)	1.47(0.06)	1.6

show similar features in the C^{18}O (3-2) line (15470-5419c1, 16061-5048c1, 16573-4214c2) except for 16482-4443c2.

In Table 5 we give the N_2H^+ (3-2) line parameters: in Cols. 3 – 7 we list integrated intensity ($\int T_{\text{MB}} dv$), peak velocity (v_{LSR}), FWHM, opacity (τ), and excitation temperature (T_{ex}) of the N_2H^+ (3-2) line, respectively. Because the rotational transitions of N_2H^+ possess hyperfine structure, we fitted the lines using the METHOD HFS of the CLASS

Table 3. Detection summary: Y = detected, N = not detected, – = not observed;

Source	APEX			ATCA (NH ₃)
	C ¹⁸ O (3–2)	N ₂ H ⁺ (3–2)	N ₂ D ⁺ (4–3)	NH ₃ (1,1) / (2,2)
08477–4359c1	Y	Y	N	Y / Y
13039–6108c6	Y	Y	N	Y / Y
13560–6133c2	Y	–	–	Y / Y
14183–6050c3	Y	–	–	Y / N
15038–5828c1	Y	–	N	Y / Y
15278–5620c2	Y	–	N	Y / Y
15470–5419c1	Y	Y	N	Y / Y
15470–5419c3	Y	Y	N	Y / Y
15557–5215c2	Y	Y	Y ^a	Y / Y
15557–5215c3	Y	Y	N	Y / Y
16061–5048c1	Y	Y	N	Y / Y
16061–5048c4	Y	Y	N	Y / Y
16093–5128c2	Y	Y	–	Y / Y
16093–5128c8	Y	–	–	Y / Y
16164–4929c3	Y	–	–	Y / Y
16254–4844c1	Y	–	–	Y / Y
16435–4515c3	Y	Y	–	Y / Y
16482–4443c2	Y	Y	–	Y / Y
16573–4214c2	Y	Y	–	Y / Y
17040–3959c1	Y	–	–	Y / Y
17195–3811c2	Y	–	–	Y / Y

^a marginal detection (see Sect. 4.4).**Table 5.** N₂H⁺ line parameters and column densities. For optically thin transitions without well-constrained opacity ($\tau = 0.1$), to compute $N(\text{N}_2\text{H}^+)$ we adopted a $T_{\text{ex}} = 6$ K (see text). For sources with more than one velocity component, the line labelled as ‘-a’ is the one having the peak velocity consistent with that of the clump of our interest, as in Table 4.

source	vel. range km s ^{−1}	$\int T_{\text{MB}} dv$ K km s ^{−1}	v_{LSR} km s ^{−1}	FWHM km s ^{−1}	τ	T_{ex} K	$N(\text{N}_2\text{H}^+)$ ($\times 10^{13}$)cm ^{−2}
08477–4359c1	5.4,14.8	6.02(0.07)	10.53(0.02)	2.87(0.05)	0.1	6	2.93(0.03)
13039–6108c6	−30.0,−23.6	0.66(0.08)	−26.2(0.1)	1.6(0.4)	0.1	6	0.32(0.04)
15470–5419c1	−66.1,−54.8	5.2(0.1)	−58.82(0.03)	2.4(0.2)	12(2)	4.8(0.3)	54(1)
15470–5419c3	−67.1,−56.8	9.4(0.1)	−61.38(0.03)	3.14(0.02)	0.1	6	4.6(0.05)
15557–5215c2	−74.1,−62.6	17.2(0.2)	−66.77(0.02)	2.01(0.05)	12.7(0.8)	8.0(0.5)	27(2)
15557–5215c3	−71.8,−66.2	1.12(0.07)	−68.69(0.06)	1.61(0.09)	1.4(0.2)	4.6(0.2)	1.8(0.1)
16061–5048c1	−72.6,−59.5	25.3(0.2)	−66.20(0.02)	3.14(0.09)	9.1(0.8)	9(1)	29(3)
16061–5048c4	−56.3,−48.3	2.13(0.08)	−51.98(0.05)	1.29(0.09)	7(1)	4.5(0.3)	18(4)
16093–5128c2–a	−102.1,−92.1	1.28(0.06)	−97.20(0.08)	3.1(0.2)	0.1	6	0.62(0.03)
16093–5128c2–b	−68.0,−60.2	0.63(0.06)	−63.21(0.08)	1.7(0.3)	0.3(1.5)	6	0.38(0.04)
16435–4515c3–a	−53.0,−49.8	0.08(0.02)	−51.1(0.3)	1.6(0.4)	0.1	6	0.04(0.01)
16435–4515c3–b	−37.1,−32.5	0.23(0.02)	−35.2(0.1)	1.5(0.3)	1(0.2)	3.5(0.7)	2.7(0.2)
16482–4443c2	−47.0,−38.6	3.68(0.07)	−42.57(0.03)	3.02(0.09)	0.1	6	1.79(0.03)
16573–4214c2	−32.5,−22.2	9.52(0.08)	−27.06(0.01)	3.79(0.02)	0.1	6	4.64(0.04)

package³. This method fits all the hyperfine components simultaneously assuming that they have the same excitation temperature and width, that the opacity has a Gaussian dependence on frequency and fixing the separation of the components to the laboratory value. The line parameters listed in Table 5 have been derived from this method, except the integrated intensity that has been computed by simple integration over the velocity range given in Col. 2. The line opacity is deduced from the intensity ratio of the different

hyperfine components, most of which are blended due to the fact that the line widths are larger ($\sim 1 - 3$ km s^{−1}) than the separation in velocity of the components. However, the fit residuals are generally low indicating that the procedure provides good results despite the blending.

4.3 Column densities of N₂H⁺

The N₂H⁺ column densities were derived following the method outlined in the Appendix A of Caselli et al. (2002a). Specifically, we adopted equations (A-1) and (A-4) for optically thick and optically thin lines, respectively. The method assumes a constant excitation temperature, T_{ex} . An estimate

³ The CLASS program is part of the GILDAS software, developed at the IRAM and the Observatoire de Grenoble, and is available at <http://www.iram.fr/IRAMFR/GILDAS>

of T_{ex} can be derived from the fitting procedure to the hyperfine structure⁴, but not for optically thin lines or lines with opacity not well-constrained. For these, we have assumed the average T_{ex} (~ 6 K; Table 5) derived for the sources with well-constrained opacity.

For all sources but 16573–4214c2 and 16482–4443c2, the clump diameter derived from the 1.2 mm continuum is comparable to or larger than the beam size (see Table 2 in Beltrán et al. 2006, see also Table 8), so that we assumed unity filling factor. This factor was applied also to the unresolved source 16482–4443c2. We stress that this is an approximation, because the sources could be clumpy. However, due to the lack of observations at higher-angular resolution, neither in the lines observed in this work nor in other high-density gas tracers, the size of the effective emitting region cannot be determined. For 16573–4214c2, for which $\theta_s \sim 7''$, we applied a correction factor $1/\eta_\nu = (\theta_s^2 + \text{HPBW}^2)/\theta_s^2 \sim 10$.

The N_2H^+ total column densities are given in Col. 8 of Table 5, and span a range from 10^{12} to 10^{14} cm^{-2} . These values are in good agreement with those derived from the same line in other IRDCs (Ragan et al. 2006, Miettinen et al. 2011), as well as in other massive starless and star-forming cores (Fontani et al. 2011, Chen et al. 2011).

4.4 Upper limits on the column density of N_2D^+ and on $\text{N}_2\text{D}^+/\text{N}_2\text{H}^+$ column density ratio

The N_2D^+ (4–3) transition was marginally detected at $\sim 3.2\sigma$ rms only towards 15557–5215c2. This represents, to our knowledge, the first detection of this line in an IRDC. The spectrum is shown in Fig. 2. For this source we have computed the N_2D^+ column density fitting the line with a Gaussian (the results are given in Table 6), and then following the approach of Appendix A in Caselli et al. (2002a) to derive the N_2D^+ column density for the optically thin case. This line is also a blend of hyperfine components, therefore the line width derived from the Gaussian fit is an upper limit to the intrinsic value. However, because of the poor signal-to-noise ratio of the spectrum, METHOD HFS did not provide reliable results. As T_{ex} , we used that derived from N_2H^+ (3–2) for this source (see Table 5). We find $N(\text{N}_2\text{D}^+) \sim 8 \times 10^{11} \text{ cm}^{-2}$ and the corresponding deuterated fraction (column density ratio $N(\text{N}_2\text{D}^+)/N(\text{N}_2\text{H}^+) = D_{\text{frac}}$) is ~ 0.003 (Table 6). This value is consistent with studies performed in both IRDCs (e.g. Miettinen et al. 2011, Chen et al. 2011) and massive star-forming clumps containing more evolved objects (e.g. Fontani et al. 2006, 2011).

For all the other undetected sources, we have derived upper limits on the deuterated fraction in between 0.003 and 0.5. These upper limits were computed from the integrated intensity upper limits assuming the lines to be Gaussian from the formula $\int T_{\text{MB}} dv = \frac{\Delta V}{2\sqrt{\ln 2/\pi}} T_{\text{MB}}^{\text{peak}}$. We adopted the 3σ rms level in the spectrum as peak temperature $T_{\text{MB}}^{\text{peak}}$, and the line width measured in the detected source 15557–5215c2 (Table 2) as ΔV . The D_{frac} upper limits are comparable to the values commonly measured in massive clumps (Fontani

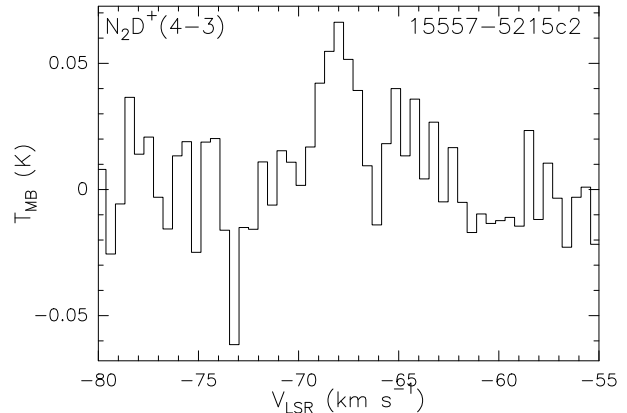


Figure 2. N_2D^+ (4–3) spectrum of the only source detected in this transition, 15557–5215c2.

et al. 2006, Chen et al. 2011, Miettinen et al. 2011), so that our sensitivity does not allow to conclude if our targets have deuterated fraction similar to or lower than the other clumps in the literature. We believe that the very low detection rate in the N_2D^+ (4–3) line is likely due to the high densities required to excite this transition: having a critical density of $\sim 3 \times 10^7 \text{ cm}^{-3}$, this line is expected to come from very compact regions, thus suffering enormous beam dilution effects.

4.5 Rotation temperatures and NH_3 column densities at dust emission peak position

We have extracted spectra of the NH_3 (1,1) and (2,2) transitions from the ATCA channel maps towards the positions given in Table 1. The spectra obtained this way were then imported in CLASS, and fitted using METHOD NH_3 to fit the (1,1) lines, which takes into account the line hyperfine structure, similarly to METHOD HFS (see Sect. 4.2). This was also used for the (2,2) emission, even though the hyperfine components were not always visible, to obtain an upper limit for τ .

In Table 7 we list the rotation temperatures (T_{rot}), kinetic temperatures (T_{k}), and total column densities of ammonia (N_{NH_3}) derived from the NH_3 (2,2)/(1,1) line ratios, as well as the line peak velocities. We have derived T_{rot} and N_{NH_3} from the output parameters given by the fitting method outlined above, and using the formulae given in the Appendix of Busquet et al. (2009). The formulae, which result from the discussion in Ho & Townes (1983, Eq. (4)), have been derived assuming that the transitions between the metastable inversion doublets are approximated as a two-level system, and that the excitation temperature and line width are the same for both NH_3 (1, 1) and NH_3 (2, 2). Note that the assumption of a two-level system is reasonable because transitions between the metastable inversion doublets are usually much faster than those of other rotational states (Ho & Townes 1983). T_{k} was extrapolated from T_{rot} following the empirical approximation method described in Tafalla et al. (2004, see also Eq. (A.5) in Busquet et al. 2009). We find kinetic temperatures in between 13 and 25 K, with both mean and median T_{k} of ~ 17 K. These values are consistent, within the errors, with typical temperatures measured towards IRDCs (Pillai et al. 2006) from ammonia.

⁴ See the CLASS user manual for the derivation of T_{ex} from the output parameters: <http://iram.fr/IRAMFR/GILDAS/doc/html/class-html/class.html/>

Table 6. N_2D^+ (4–3) line parameters and N_2D^+ column density in 15557–5215c2

$\int T_{\text{MB}} dv$ K km s ⁻¹	v_{LSR} km s ⁻¹	FWHM km s ⁻¹	T_{peak} K	$N(\text{N}_2\text{D}^+)$ ($\times 10^{11}$) cm ⁻²	$N(\text{N}_2\text{D}^+)/N(\text{N}_2\text{H}^+)$
0.14(0.03)	-68.1(0.2)	2.0(0.5)	0.07	8(2)	0.003(0.001)

Table 7. Rotation temperature, kinetic temperature, total NH_3 column densities and peak velocities derived from the NH_3 inversion transitions observed with the ATCA. The errors on T_{rot} and T_{k} are given in parentheses and are computed from the propagation of errors. The uncertainty on the column densities includes the error on the flux calibration, and is estimated to be of the order of 20 – 30%.

Source	T_{rot}	T_{k}	N_{NH_3}	V_{peak}^a
	K	K	10^{15} cm ⁻²	km s ⁻¹
08477–4359c1	16(2)	19(3)	1.06	+11.18(0.02)
13560–6133c2	15(9)	17(10)	4.61	-56.32(0.05)
14183–6050c3 ^b	–	–	–	-44.36(0.04)
15038–5828c1	14(3)	15(4)	2.97	-68.72(0.04)
15278–5620c2	17(2)	20(3)	3.52	-48.69(0.02)
15470–5419c1–a	16(2)	18(3)	4.23	-60.72(0.03)
15470–5419c1–b	13(9)	14(9)	3.20	-57.88(0.06)
15470–5419c3	17(1)	19(2)	3.61	-61.02(0.01)
15557–5215c2	19(2)	23(4)	4.62	-67.11(0.01)
15557–5215c3	14(3)	15(3)	4.47	-68.53(0.01)
16061–5048c1	20(3)	25(5)	4.44	-66.76(0.01)
16061–5048c4	12(2)	13(2)	5.28	-51.62(0.01)
16093–5128c2	14(5)	16(5)	3.87	-97.09(0.05)
16093–5128c8	14(6)	15(7)	1.09	-95.80(0.04)
16164–4929c3	13(6)	14(6)	2.59	-32.80(0.01)
16254–4844c1 ^c	18(4)	22(6)	4.77	-38.45(0.05)
16435–4515c3	11(4)	12(5)	1.84	-51.69(0.04)
16482–4443c2	15(3)	16(4)	0.78	-42.35(0.03)
16573–4214c2 ^c	15(4)	17(5)	3.32	-25.09(0.04)
17040–3959c1	16(3)	18(4)	6.81	-15.62(0.02)
17195–3811c2	15(1)	17(2)	1.13	-25.51(0.01)

^a derived from the (1,1) transition. The uncertainty (between parentheses) is that given by the fitting procedure;

^b undetected in the (2,2) transition (see Table 3);

^c observed only for one cycle with bad UV coverage. The values listed have been derived from the spectra extracted from the dirty map deconvolved with the dirty beam.

4.6 H_2 masses and other physical parameters from 1.2 mm continuum emission

Gas masses were calculated by Beltrán et al. (2006) for all clumps from the 1.2 mm continuum integrated flux density, assuming optically thin emission and a reasonable dust temperature of 30 K for all clumps. This latter assumption was due to the fact that a temperature estimate for each clump was lacking. In this work we can profit from the temperatures derived from ammonia (Col. 3 of Table 7) and recompute the H_2 masses assuming that the dust temperature equals the kinetic temperature. This method implies coupling between gas and dust, which is a realistic assumption for gas densities as those of our clumps ($\geq 10^4$ cm⁻³).

The gas mass, M , has been derived using Eq. (1) in Beltrán et al. (2006), and adopting the same assumptions,

except the dust temperature for which we have utilised T_{k} derived from ammonia. From M , for each source we have calculated the source averaged H_2 volume and column densities, n_{H_2} and $N_{\text{t}}(\text{H}_2)$, assuming the clumps to be spherical and homogeneous. The H_2 column densities, $N_{\text{p}}(\text{H}_2)$, have been estimated also from the 1.2 mm continuum peak flux using the equations in Beuther et al. (2002) and adopting the same assumptions made to derive the mass (same β , dust mass opacity and gas-to-dust ratio). These represent average values in the telescope beam of the 1.2 mm continuum observations ($\sim 24''$), and we will use these estimates to derive the CO depletion in Sect. 4.7, because the APEX C¹⁸O observations have a comparable angular resolution ($\sim 19''$). Also, we have computed the source averaged surface density, $\Sigma(\text{H}_2) = 4M/\pi(\theta_{\text{s}}d)^2$, where d and θ_{s} are the source distance (see Table 1) and angular diameter (see Table 8), respectively. For 16435–4515c3, for which we did not have a kinematic source distance, we computed it from the velocity of the C¹⁸O (3–2) line of the ‘a’ component (see Table 4) following the method explained in Fontani et al. (2005). The method, which assumes the rotation curve of Brand & Blitz (1993), is valid for distances from the Galactic centre between 2 and 25 kpc, and provides two kinematic distances, 3.1 and 12.6 kpc. As for the other sources with distance ambiguity, we adopted the ‘near’ value, i.e. 3.1 kpc.

The results are listed in Table 8, where we give M , n_{H_2} , $N(\text{H}_2)$ (both $N_{\text{t}}(\text{H}_2)$ and $N_{\text{p}}(\text{H}_2)$) and $\Sigma(\text{H}_2)$. For completeness, in Cols. 2 and 3 of Table 8 we list the full width half maximum diameters, θ_{s} (deconvolved with the telescope beam of $24''$) adopted to derive n_{H_2} , $N_{\text{t}}(\text{H}_2)$ and $\Sigma(\text{H}_2)$, as well as the integrated flux densities used to calculate the masses, S_{ν} . Both parameters are taken from Beltrán et al. (2006). The mean mass turns out to be 439 M_{\odot} , and the median is 244 M_{\odot} . As expected, these values are systematically higher than those derived by Beltrán et al. (2006) given that the kinetic temperatures from ammonia (see Table 7) are systematically lower than the representative value (30 K) assumed by Beltrán et al. (2006). The clump-averaged column densities are of the order of $10^{22} - 10^{23}$ cm⁻², with a mean value of 1.6×10^{23} cm⁻² and a median of 8.5×10^{22} cm⁻². The volume densities are of the order of $10^4 - 10^5$ cm⁻³, with a mean value of 3.1×10^5 cm⁻³ and a median of 3.9×10^4 cm⁻³. Finally, the mean surface density is 0.37 g cm⁻², and its median value is 0.19 g cm⁻². The difference between mean and median values for all parameters is due to the clump 16573–4214c2, which has an angular diameter ($\sim 7''$) more than twice smaller than any other source of the sample, despite the comparable mass.

The clump-averaged column densities $N_{\text{t}}(\text{H}_2)$ are generally smaller than the theoretical threshold given by Krumholz & McKee (2008) to avoid cloud fragmentation, which is ~ 1 g cm⁻², corresponding to $\sim 3 \times 10^{23}$ cm⁻². Also, the distance independent parameter $\Sigma(\text{H}_2)$ is smaller, on average, than the theoretical values predicted for clumps

that are going to form high-mass stars or super star clusters, which are expected to be larger than $\sim 0.7 \text{ g cm}^{-2}$ (Chakrabarti & McKee 2005, Krumholz & McKee 2008). Rather, the values measured in this work are consistent to those predicted for clumps that are going to form intermediate-mass stars and stellar clusters (Chakrabarti & McKee 2005). We stress, however, that $\Sigma(\text{H}_2)$ and $N_t(\text{H}_2)$ represent average values across the whole clumps, which could in reality be fragmented in smaller and denser cores. Therefore, our $\Sigma(\text{H}_2)$ and $N_t(\text{H}_2)$ are to be considered as lower limits for the individual embedded cores. On the other hand, the column densities calculated from the 1.2 mm continuum peak flux, $N_p(\text{H}_2)$, are closer to the theoretical threshold proposed by Krumholz & McKee (2008), indicating that the central regions of the clumps could more easily form massive stars. Moreover, we have compared the clump masses to the threshold proposed by Kauffmann & Pillai (2010) based on an empirical mass-radius relation which predicts that a cloud must exceed the relation $M > M_{\text{thr}} = 870 M_\odot (R/\text{pc})^{1.33}$ to form massive stars. The mass thresholds M_{thr} are listed in Col. 9 of Table 8. As R , we have used half of the diameters listed in the same Table. We can see that our clump masses are all above the predicted threshold, with four exceptions: 13039–6108c6, 15557–5215c3, 16164–4929c3 and 16482–4443c2, for which, in any case, the measured mass and the corresponding threshold value are similar, and for 16482–4443c2 the mass threshold is even an upper limit. Based on these results, we claim that the targets have the potential to form massive stars.

4.7 C^{18}O column densities and CO depletion factors

The C^{18}O column density has been derived from line intensities assuming optically thin lines and LTE conditions. Under these assumptions one can demonstrate that the total column density of C^{18}O , $N_{\text{C}^{18}\text{O}}$, is related to the integrated intensity of a rotational transition $J \rightarrow J-1$ according to (e.g. Pillai et al. 2007):

$$N_{\text{C}^{18}\text{O}} = \frac{N_J}{g_J} Q(T_{\text{ex}}) e^{\left(\frac{E_J}{kT_{\text{ex}}}\right)} = \frac{3h}{8\pi^3 S \mu^2} \frac{1}{J_\nu(T_{\text{ex}}) - J_\nu(T_{\text{BG}})} \frac{I(\text{C}^{18}\text{O})}{e^{h\nu/kT_{\text{ex}}} - 1} \frac{1}{\eta_\nu} \quad (1)$$

where: $I(\text{C}^{18}\text{O})$ is the integrated intensity of the line; N_J is the column density of the upper level; g_J , E_J and S are statistical weight ($=2J+1$), energy of the upper level and line strength, respectively; $Q(T_{\text{ex}})$ is the partition function at the temperature T_{ex} ; ν the line rest frequency; $J_\nu(T_{\text{ex}})$ and $J_\nu(T_{\text{BG}})$ the equivalent Rayleigh-Jeans temperatures at frequency ν computed for the excitation and background temperature ($T_{\text{BG}} \sim 2.7 \text{ K}$), respectively; μ the molecule's dipole moment (0.1102 Debye for C^{18}O); η_ν the beam filling factor. The total integrated intensity $I(\text{C}^{18}\text{O})$ was derived from the integral over all the channels with emission instead of the area given by the Gaussian fits to take into account also non-Gaussian features.

As for the derivation of the N_2H^+ column density, we assumed a unity filling factor for all sources, so that $N_{\text{C}^{18}\text{O}}$ is a beam-averaged value. As excitation temperature, we have used the kinetic temperatures listed in Col. 3 of Table 7

(i.e. we are assuming LTE conditions for C^{18}O (3–2)). The resulting column densities are listed in Table 9. To check if the assumption of optically thin lines is reasonable, we have estimated the line optical depths from the solution of the line radiative transfer equation:

$$\tau = -\ln \left(1 - \frac{T_{\text{MB}}}{J_\nu(T_{\text{ex}}) - J_\nu(T_{\text{BG}})} \right)$$

and found values smaller than $\simeq 0.6$, consistent with our assumption of optically thin lines.

The CO depletion factor, f_{D} , is defined as the ratio between the 'expected' abundance of CO relative to H_2 ($X_{\text{C}^{18}\text{O}}^E$) and the 'observed' value:

$$f_{\text{D}} = \frac{X_{\text{C}^{18}\text{O}}^E}{X_{\text{C}^{18}\text{O}}^O} \quad (2)$$

$X_{\text{C}^{18}\text{O}}^O$ is the ratio between the observed C^{18}O column density and the observed H_2 column density. For this latter, we have used the value derived from the 1.2 mm continuum peak flux, $N_p(\text{H}_2)$ (Col. 7 of Table 8), which is averaged over a beam comparable to that of the C^{18}O observations (24'' against 19'').

To compute $X_{\text{C}^{18}\text{O}}^E$, we have taken into account the variation of atomic carbon and oxygen abundances with distance to the Galactic Center following the same procedure adopted in Fontani et al. (2006; see also Miettinen et al. 2011). Assuming the canonical abundance of $\sim 8.5 \times 10^{-5}$ for the abundance of the main CO isotopologue in the neighbourhood of the solar system (Frerking et al. 1982, see also Langer et al. 1989 and Pineda et al. 2008), we have computed the expected CO abundance at the Galactocentric distance (D_{GC}) of each source according to the relationship:

$$X_{\text{C}^{16}\text{O}}^E = 8.5 \times 10^{-5} \exp(1.105 - 0.13 D_{\text{GC}}(\text{kpc})) \quad (3)$$

which has been derived according to the abundance gradients in the Galactic Disk for $^{12}\text{C}/\text{H}$ and $^{16}\text{O}/\text{H}$ listed in Table 1 of Wilson & Matteucci (1992), and assuming that the Sun has a distance of 8.5 kpc from the Galactic Centre. Then, following Wilson & Rood (1994), we have assumed that the Oxygen isotope ratio $^{16}\text{O}/^{18}\text{O}$ depends on D_{GC} according to the relationship $^{16}\text{O}/^{18}\text{O} = 58.8 \times D_{\text{GC}}(\text{kpc}) + 37.1$, which gives:

$$X_{\text{C}^{18}\text{O}}^E = \frac{X_{\text{C}^{16}\text{O}}^E}{(58.8 D_{\text{GC}} + 37.1)} \quad (4)$$

The results are listed in Table 9: Cols. 2, 3 and 4 list the C^{18}O (3–2) integrated line intensity ($I(\text{C}^{18}\text{O})$), the C^{18}O column density ($N(\text{C}^{18}\text{O})$) and the observed C^{18}O abundance ($X_{\text{C}^{18}\text{O}}^O$); Cols. 5 and 6 give the expected C^{18}O abundance ($X_{\text{C}^{18}\text{O}}^E$) calculated at the Galactocentric distance of the source (Table 1) and the CO depletion factor ($f_{\text{D}} = X_{\text{C}^{18}\text{O}}^E/X_{\text{C}^{18}\text{O}}^O$), respectively.

The mean f_{D} is ~ 32 and the median value is 29. These values are remarkably higher than those obtained in other IRDCs (Pillai et al. 2007, Miettinen et al. 2011, Hernández et al. 2011), and are among the highest obtained both in low-mass starless cores (Crapsi et al. 2005, Tafalla et al. 2006) and in massive clumps from observations with low-angular resolution (Fontani et al. 2006, Chen et al. 2011).

Such a difference could be explained by the fact that the transition used in this work to derive f_{D} has a critical density of $\sim 5 \times 10^4 \text{ cm}^{-3}$, comparable to that of the

Table 8. Parameters derived from the 1.2 mm continuum emission: 1.2 mm continuum flux density (S_ν) integrated over the 3σ rms contour level, clump angular diameter (θ_s), gas mass (M), H_2 volume (n_{H_2}), column ($N(H_2)$) and mass surface density ($\Sigma(H_2)$). The last column lists the mass threshold, M_{thr} , for a cloud that can form massive stars based on the empirical mass-radius relation proposed by Kauffmann & Pillai (2010, see text).

source	S_ν^a (Jy)	θ_s^b (")	M (M_\odot)	n_{H_2} ($\times 10^4 \text{ cm}^{-3}$)	$N_t(H_2)^c$ ($\times 10^{22} \text{ cm}^{-2}$)	$N_p(H_2)^d$ ($\times 10^{23} \text{ cm}^{-2}$)	$\Sigma(H_2)$ (g cm^{-2})	M_{thr} (M_\odot)
08477–4359c1	1.8	35.6	86.73	11.5	11.0	1.42	0.24	73
13039–6108c6	1.04	40.3	101.5	3.90	5.64	0.68	0.12	127
13560–6133c2	0.77	23.8	426.8	6.27	12.5	1.09	0.27	194
14183–6050c3	1.06	39.6	207.7	2.96	5.95	0.68	0.13	196
15038–5828c1	0.49	24.7	250.6	4.62	8.53	0.85	0.19	175
15278–5620c2	1.5	40.1	243.7	3.34	6.81	0.82	0.15	200
15470–5419c1	1.16	24.2	310.2	11.0	16.4	1.37	0.36	131
15470–5419c3	3.06	54.1	743.4	2.37	7.84	1.11	0.17	382
15557–5215c2	2.89	41.3	633.4	3.67	9.96	1.55	0.22	293
15557–5215c3	0.51	35.8	194.3	1.73	4.07	0.49	0.09	242
16061–5048c1	2.1	28.1	284.3	9.54	14.4	1.66	0.31	134
16061–5048c4	1.57	62.8	504.2	1.52	5.12	1.22	0.11	391
16093–5128c2	0.67	39.6	481.6	1.19	4.29	0.92	0.09	427
16093–5128c8	0.86	40.1	642	1.52	5.57	0.68	0.12	434
16164–4929c3	0.35	36.2	54.79	2.28	3.21	1.50	0.07	122
16254–4844c1	1.15	20.3	164.2	17.4	17.9	1.43	0.39	81
16435–4515c3	0.51	17.7	147	30.9	25.3	1.20	0.55	61
16482–4443c2	0.24	$\ll 24^e$	59.08	$\gg 3.81^e$	$\gg 4.63^e$	0.66	$\gg 0.10^e$	$\ll 101^e$
16573–4214c2	0.93	7.29	108.3	553	157	1.89	3.4	14
17040–3959c1	0.81	16.6	3428	5.80	23.7	1.60	0.52	505
17195–3811c2	2.61	44.3	597.9	5.12	12.2	1.77	0.27	246

^a from Beltrán et al. (2006);

^b full width half maximum angular diameters deconvolved with the telescope beam, from Beltrán et al. (2006);

^c computed from the total clump mass (see text);

^d computed from the 1.2 mm continuum peak flux (see text);

^e unresolved in the SIMBA map. Therefore, n_{H_2} , $N_t(H_2)$ and $\Sigma(H_2)$ are lower limits, and M_{thr} is an upper limit.

central region where the CO freeze-out is expected to be important. In fact, the CO freeze-out timescale, which depends on the H_2 volume density, becomes shorter than the free-fall timescale at densities larger than a few 10^4 cm^{-3} (see e.g. Bergin & Tafalla 2007, Caselli 2011). On the contrary, in most of the studies performed so far f_D was derived from the CO (1–0) or (2–1) lines, which trace lower-density gas where CO is significantly non-depleted, resulting in values of f_D smaller than or comparable to ~ 10 (e.g. Crapsi et al. 2005, Tafalla et al. 2006, Pillai et al. 2007). However, the discussion of this result requires three main comments. First, the values of the ‘canonical’ CO abundance measured by other authors in different objects vary by a factor of 2 (see e.g. Lacy et al. 1994; Alves et al. 1999), but because the value assumed by us was derived from the Taurus star forming regions (Frerking et al. 1982) and used in previous estimates (Crapsi et al. 2005; Emprechtinger et al. 2009), it is likely the most appropriate to make comparison with low-mass dense cores. Second, the angular resolution of our observations allows us to derive only average values of f_D over angular regions much larger than the typical fragmentation scales (few arcseconds at the distance of our targets), which in reality may have complex structures, so that our estimates should be considered as lower limits. Finally, high depletion of $C^{18}O$ could be due to mechanisms other than freeze-out in regions where young stellar objects are embedded, and can decrease the CO abundance even in warm environments (for a detailed explanation, see Fuente et al. 2012). This

comment especially concerns the clumps where the average kinetic temperature exceeds the CO sublimation temperature of $\sim 20 \text{ K}$.

5 DISCUSSION

5.1 Virial state of the clumps

In order to investigate if our targets are gravitationally stable, we have computed the virial masses of the clumps assuming virial equilibrium and negligible contributions of magnetic field and surface pressure. Assuming also that the cores are spherical, one can demonstrate that the gas mass is given by:

$$M_{\text{vir}}(M_\odot) \simeq k \Delta v^2 (\text{km s}^{-1}) R(\text{pc}) , \quad (5)$$

where R is the clump radius, Δv^2 the line width and k is a multiplicative factor that depends on the gas density distribution as a function of the distance to the clump centre (see Eq. (3) in MacLaren et al. 1988). For a homogeneous clump (i.e. $\rho = \text{const.}$), $k \simeq 210$, while for $\rho \sim r^{-2}$, $k \simeq 126$. The millimetre continuum maps do not allow to derive the density profile of the clumps because of the low angular resolution and sensitivity to extended emission. However, previous studies suggest that the density structure of massive clumps reasonably can be approximated by a constant density in the inner regions, and by a steep power-law in the outer lay-

Table 9. Parameters used to determine the CO depletion factor: integrated intensity of the C¹⁸O (3–2) line ($I(\text{C}^{18}\text{O})$), C¹⁸O total column density ($N(\text{C}^{18}\text{O})$), observed C¹⁸O abundance ($X_{\text{C}^{18}\text{O}}^O$), ‘expected’ C¹⁸O abundance ($X_{\text{C}^{18}\text{O}}^E$), and CO depletion factor ($f_D = X_{\text{C}^{18}\text{O}}^E/X_{\text{C}^{18}\text{O}}^O$). The errors are given between parentheses. The uncertainty on f_D based on the calibration errors affecting the C¹⁸O and H₂ column densities is of the order of the 40–50%.

source	$I(\text{C}^{18}\text{O})$ (K km s ^{−1})	$N(\text{C}^{18}\text{O})$ ($\times 10^{15}\text{cm}^{-2}$)	$X_{\text{C}^{18}\text{O}}^O$ ($\times 10^{-8}$)	$X_{\text{C}^{18}\text{O}}^E$ ($\times 10^{-7}$)	f_D
08477–4359c1	6.5(0.1)	3.03(0.05)	2.14	1.45	7
13039–6108c6	1.5(0.2)	0.65(0.09)	0.95	2.08	22
13560–6133c2	1.8(0.1)	1.08(0.06)	0.99	2.68	27
14183–6050c3	0.9(0.1)	0.41(0.04)	0.60	2.54	42
15038–5828c1	0.89(0.09)	0.52(0.05)	0.61	3.30	54
15278–5620c2	2.5(0.1)	1.10(0.04)	1.34	2.93	22
15470–5419c1	2.3(0.1)	1.36(0.06)	0.99	3.46	35
15470–5419c3	2.6(0.1)	1.06(0.04)	0.96	3.46	36
15557–5215c2	4.2(0.1)	1.90(0.04)	1.20	3.79	32
15557–5215c3	1.6(0.1)	0.76(0.05)	1.57	3.79	24
16061–5048c1	8.8(0.2)	4.7(0.1)	2.83	3.39	12
16061–5048c4	3.0(0.1)	1.23(0.04)	1.01	3.39	34
16093–5128c2–a	3.55(0.08)	1.59(0.04)	1.72	5.09	29
16093–5128c8	1.00(0.06)	0.44(0.03)	0.65	5.09	78
16164–4929c3	3.01(0.07)	1.40(0.03)	0.93	2.80	30
16254–4844c1	2.82(0.09)	1.93(0.06)	1.35	3.39	25
16435–4515c3–a	1.73(0.09)	0.68(0.07)	0.57	4.13	73
16482–4443c2	4.7(0.1)	2.96(0.06)	4.45	3.87	9
16573–4214c2	7.8(0.1)	2.2(0.3)	1.18	2.98	25
17040–3959c1	6.32(0.09)	5.32(0.08)	3.32	1.59	5
17195–3811c2	3.07(0.08)	1.33(0.03)	0.75	4.04	54

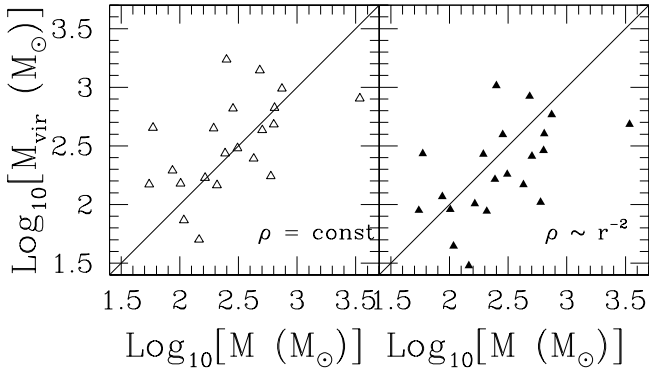


Figure 3. Virial masses against gas masses computed from the 1.2 mm dust continuum emission. M_{VIR} is calculated assuming a density distribution of the type $\rho = \text{const.}$ (left panel) and $\rho \sim r^{-2}$ (right panel). In both panels, the line indicates $M_{\text{VIR}} = M$.

In Fig. 3 we compare the mass derived from the dust continuum emission to M_{VIR} obtained assuming $\rho \sim \text{const.}$ (left panel) and $\rho \sim r^{-2}$ (right panel). We note that M_{VIR} is on average larger than M for the case $\rho \sim \text{const.}$, while it is on average smaller for the other case. Because the overall density distribution of the clumps is likely in between these two extreme cases, we suggest that, on average, the clumps are close to virial equilibrium. Our findings are in good agreement with those derived by López-Sepulcre et al. (2010) in a sample of high-mass clumps supposed to span a wide range of evolutionary stages. The gas masses of the high-mass clumps studied by López-Sepulcre et al. (2010) were derived from millimetre continuum measurements, and the dust temperatures assumed are in agreement with ours (see their Table 1). Moreover, they estimated the virial masses from C¹⁸O (2–1) line widths and assuming $\rho \sim \text{const.}$ As shown in Fig. 4, we do not highlight systematic differences between the two sub-samples, and between infrared-dark and infrared-bright sources either. On average, the sources of the López-Sepulcre et al.’s sample appear to have slightly larger virial masses, so that potentially they might be less gravitationally bound than the clumps studied in this work. However, we stress that the parameters from which the mass estimates are derived are affected by large errors (especially the dust mass opacity, the distance and the gas-to-dust ratio) and difficult to quantify. For example, the dust mass opacity coefficient can introduce a factor 2 in the uncertainty (Beuther et al. 2002). Hence our conclusions on the virial stability of the targets must be taken with caution.

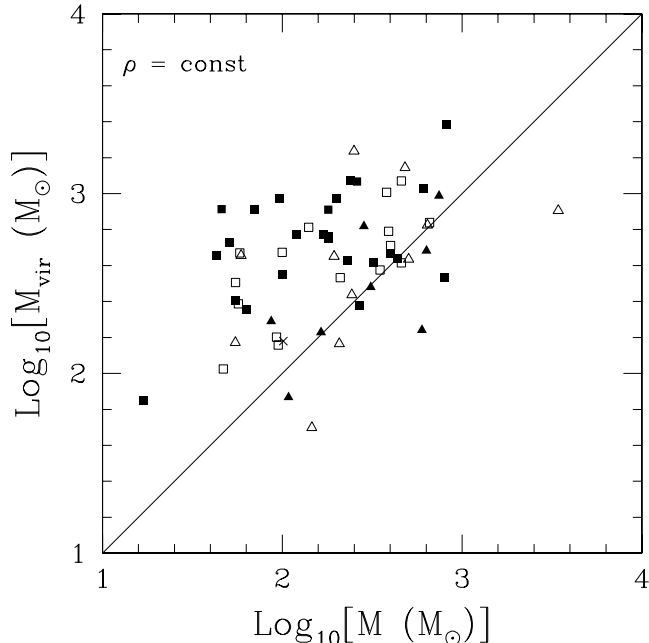


Figure 4. Virial masses against gas masses computed from the dust continuum emission for the clumps studied in this work (triangles) and the massive clumps observed by López-Sepulcre et al. (2010, squares). Filled and open triangles represent sources detected and undetected at 24 μm , respectively, while the filled and open squares represent the infrared-bright and infrared-dark sources selected by López-Sepulcre et al. (2010), respectively. The cross indicates the clump with no 24 μm image available, 13039–6108c6. M_{VIR} is calculated assuming homogeneous clumps. The line indicates $M_{\text{VIR}} = M$.

5.2 24 μm dark versus 24 μm bright clumps

The presence of mid-infrared emission in molecular clumps is very often the sign of embedded star formation activity. Therefore, the IRDCs detected at 24 μm could harbour objects more evolved than those undetected. If this is the case, the two groups should have physical properties indicative of a different evolutionary stage. In Fig. 5 we show histograms which compare some physical and chemical properties of the IRDCs detected and undetected at 24 μm : line widths, kinetic temperature, column ($N_t(\text{H}_2)$), volume and surface density of H_2 , gas masses (both from continuum and the virial theorem), CO depletion factor and clump diameter. For M_{VIR} , we have considered the values calculated assuming $\rho \sim \text{const}$, bearing in mind that those obtained in the case $\rho \sim r^{-2}$ are just systematically lower by a factor ~ 1.7 . For the unresolved source 16482–4443c2, we have not included the $n(\text{H}_2)$ and $\Sigma(\text{H}_2)$ lower limits, and replaced $N_t(\text{H}_2)$ with $N_p(\text{H}_2)$. Although the statistics is poor because the two sub-samples contain eight 24 μm bright and twelve 24 μm dark objects, the comparative histograms are useful to check if one can notice clear systematic differences. An inspection of the comparative histograms indicates that the 24 μm dark clumps have lower T_k and higher f_D . In fact, the average T_k and f_D of the infrared-bright group turns out to be ~ 20 K and 28, respectively, while that of the infrared-dark group is ~ 16 K and 35, respectively. Also, if we exclude from the statistical analysis the clear outliers 17040–3959c1 and 16573–4214c2, the 24 μm dark clumps

tend to have lower mass (average M of $\sim 260 M_\odot$ from the 1.2 mm continuum), smaller source-averaged H_2 column density (average $N_t(\text{H}_2)$ of $8.9 \times 10^{22} \text{ cm}^{-2}$), and smaller H_2 surface density (average $\Sigma(\text{H}_2)$ of 0.19 gr cm^{-2}) than the infrared-bright clumps (average M of $\sim 370 M_\odot$, average $N_t(\text{H}_2)$ of $1.3 \times 10^{23} \text{ cm}^{-2}$, average $\Sigma(\text{H}_2)$ of 0.27 g cm^{-2}).

The fact that on average the group of the 24 μm -dark sources has lower T_k and higher CO depletion factor than the 24 μm -bright objects suggests that it likely contains objects less evolved, and this is in accordance with other comparative studies of massive clumps with or without indications of embedded star formation (Hill et al. 2005). However, the dark sources also have lower M and H_2 column and surface density, and this could indicate that the 24 μm dark clumps may be destined to form less massive stars/clusters, thus explaining the non-detection at mid-infrared wavelengths, although material could still be accreting.

5.3 Relation between T_k and line widths

Two indicators of active star formation are the line width and the gas temperature, which are both expected to become higher with increasing star formation activity. In fact, the line widths of dense gas tracers are found to be higher in more evolved star-forming clumps than in quiescent regions of infrared-dark clouds (e.g. Hill et al. 2010, Ragan et al. 2012), while the cores associated with protostars are on average warmer than the starless cores, both in low- and high-mass star forming regions (e.g. Foster et al. 2009, Emsprecht et al. 2009, Ragan et al. 2011). Fig. 6 shows that there is a slight correlation between T_k and the C^{18}O line width. If we exclude from the statistical analysis 15038–5828c1, for which ΔV is much higher than that of the other targets and has a spectrum with poor S/N (see Fig. B2), a linear least square fit to the data yields a slope of ~ 0.09 . Statistical correlation between T_k and line width can be investigated also through non-parametric statistical methods, like the Kendall's τ correlation coefficient. This measures the rank correlation, namely how two quantities are ordered similarly when ranked by each of them⁵. τ can range between 1 (perfect agreement between the two rankings) and -1 (one ranking is the reverse of the other). We find $\tau \sim 0.23$ between T_k and line width. These results suggest a faint correlation between the two parameters, which indicates that the warmer clumps tend to also have larger line widths, i.e. tend to be more turbulent. However, the large dispersion cannot allow us to draw any firm conclusion.

5.4 Relation between CO depletion and other physical parameters

One of the main results of this work is the high CO depletion factor measured in our targets, with values higher than those found in comparable high-mass clumps (e.g. Miettinen et al. 2011, Chen et al. 2011), and even in low-mass pre-stellar cores (see e.g. Crapsi et al. 2005). The fact that we have derived f_D from the C^{18}O (3–2) transition, which has a critical density of $5 \times 10^4 \text{ cm}^{-3}$, certainly makes the

⁵ for details see, e.g., <http://www.statsoft.com/textbook/nonparametric-statistics/>

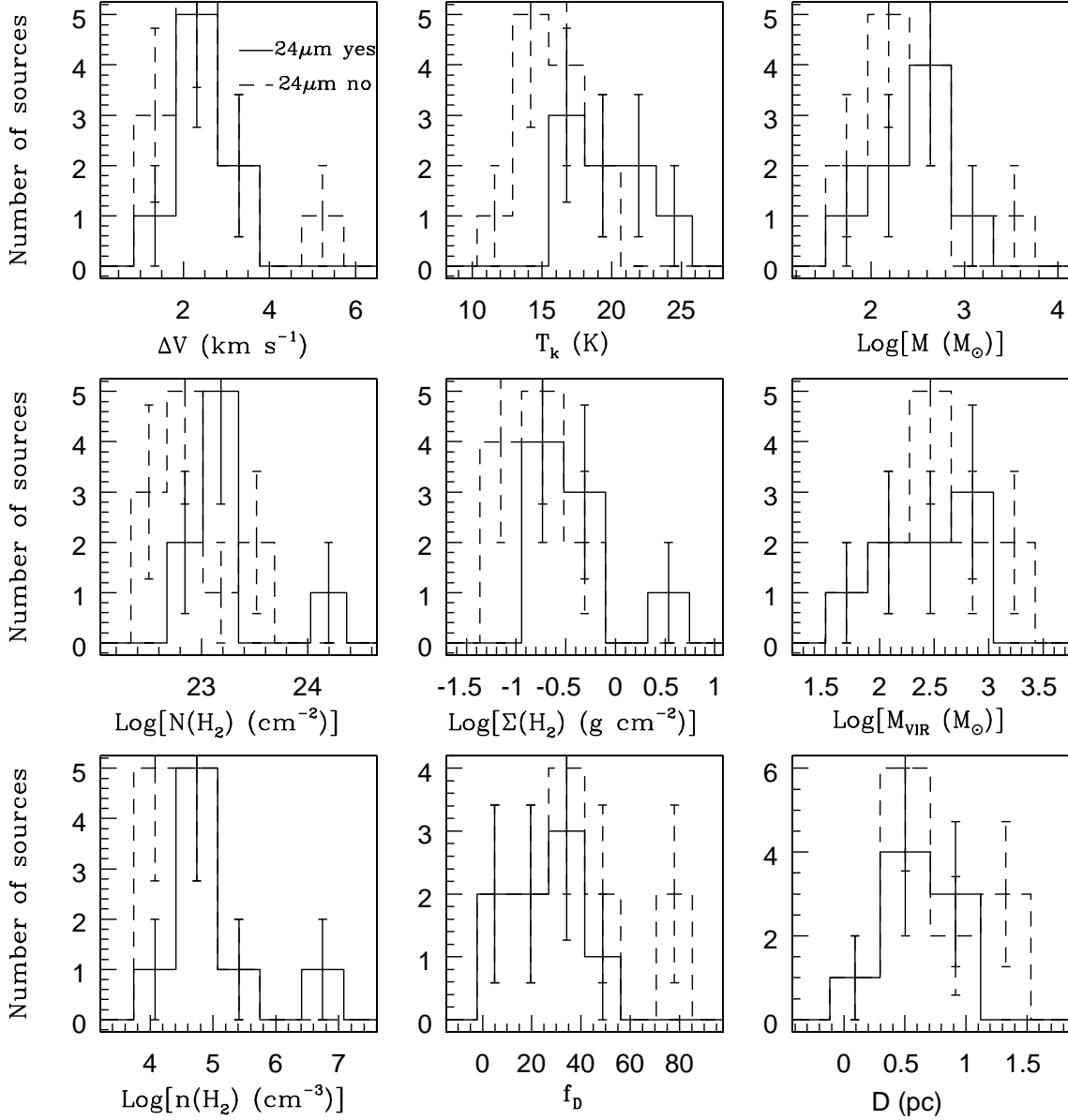


Figure 5. Histograms comparing some of the physical and chemical properties of the clumps detected (solid line) and undetected (dashed line) in the Spitzer-MIPS 24 μm image (see Figs. A1). In the panels showing $N(\text{H}_2)$, $n(\text{H}_2)$ and $\Sigma(\text{H}_2)$ we have not included the lower limits calculated for 16482–4443c2.

difference with respect to previous works in which f_D was calculated from the lower excitation transitions tracing material where freeze-out of CO is expected to be less important. In fact, freeze-out of CO and other neutrals onto dust grains is favoured in gas characterised by low temperatures ($T \leq 20$ K) and high densities ($n \geq 10^5$ cm^{-3}), in which the freeze-out timescale is generally shorter than the free-fall timescale (e.g. Bergin & Tafalla 2007). In fact, high CO depletion factors (of the order of 10 or more) were measured towards the dense and cold nuclei of low-mass pre-stellar cores (see e.g. Crapsi et al. 2005). After the formation of the protostellar object(s) at the core centre, evaporation of CO starts and the CO depletion factor drops (Caselli et al. 2002b). This theoretical prediction has been partly confirmed by observations of both low- and high-mass dense cores (e.g. Emprechtinger et al. 2009, Fontani et al. 2006).

In Fig. 7 we show f_D against T_k (in the left panel) and $n(\text{H}_2)$ (in the right panel). At a first glance, the two plots do not reveal clear (anti-)correlations between the parameters. As made in Sect. 5.3, we have performed a closer inspection of the data using the non-parametric ranking statistical test Kendall’s τ (see Sect. 5.3). If we consider all points, we find a faint anti-correlation between f_D and T_k (Kendall’s $\tau = -0.34$) and also between f_D and $n(\text{H}_2)$ (Kendall’s $\tau = -0.12$). The anti-correlation between T_k and f_D is consistent with the increase of CO depletion with decreasing temperature, as already found in both low- and high-mass dense cores (Emprechtinger et al. 2009, Fontani et al. 2006), while that between f_D and $n(\text{H}_2)$ is the opposite of what expected from chemical models. Even if we exclude from the statistical analysis 16573–4214c2, which has $n(\text{H}_2)$ markedly much higher than that of the other members of the sample, the

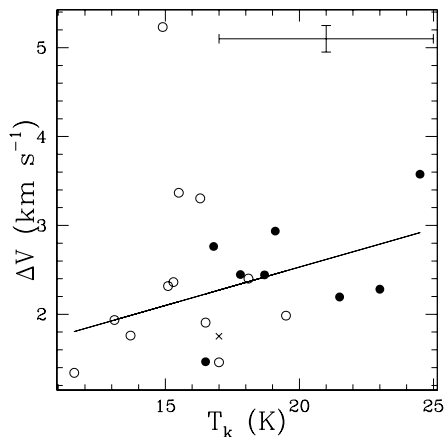


Figure 6. Gas kinetic temperature, T_k , derived from ammonia, against the $C^{18}O$ line widths, ΔV . The straight line is a least square fit to the data excluding 15038–5828c1, the clump with $\Delta V > 5 \text{ km s}^{-1}$, i.e. much higher than any other clump and based on a very noisy spectrum (see Fig. B2). The slope of the linear fit is ~ 0.09 . Filled and open symbols represent clumps detected and undetected at $24 \mu\text{m}$, respectively. The cross indicates the clump with no $24 \mu\text{m}$ image available, 13039–6108c6. Typical errorbars are depicted in the top-right corner.

correlation between f_D and $n(\text{H}_2)$ is not observed (Kendall’s $\tau = -0.11$). We point out, however, that all the parameters obtained are average values over angular regions much larger than the size expected for the embedded condensations, while the correlations are predicted for single cores. Moreover, clumps embedded in different clouds may be affected by different environmental conditions, so increasing the dispersion. In fact, Emprechtinger et al. (2009) found that dense cores in Perseus showed the best trends between the physical parameters, whereas when including cores from other star-forming regions the dispersion was significantly larger.

Finally, Fig. 8 suggests that f_D is not clearly (anti-)correlated to either the clump mass M and the ratio M_{VIR}/M which should show the tendency of a clump to be stable against gravitational collapse. When excluding the clear outlier 17040–3959c1 (whose mass is statistically much larger than the rest of the sample), a slight correlation is found between f_D and M (Kendall’s $\tau = 0.4$). However, again the large dispersion of the data and the big errors on both parameters do not allow us to claim firm conclusions.

6 CONCLUSIONS

We have undertaken a molecular line study, through observations of $C^{18}O$ (3–2), NH_3 (1,1) and (2,2), N_2H^+ (3–2) and N_2D^+ (4–3), of 21 IRDCs in the southern hemisphere with the aim of characterising the initial conditions of the high-mass star and cluster formation process. The sample targeted was selected from the high-mass millimetre clumps not detected in the MSX images identified by Beltrán et al. (2006), and includes sources with and without Spitzer $24 \mu\text{m}$ emission. The NH_3 inversion transitions have been observed with the ATCA. The rotational transitions of the other molecular species have been observed with the APEX

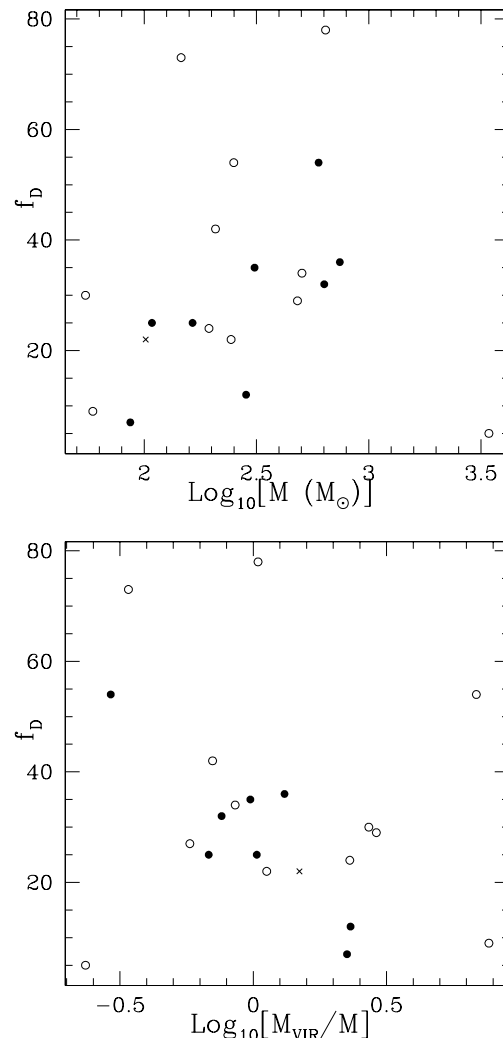


Figure 8. CO depletion factor (f_D) against gas mass derived from the 1.2 mm continuum (top panel) and M_{VIR}/M mass ratio (bottom panel). The symbols have the same meaning as in Fig. 6.

Telescope. We have detected $C^{18}O$ and ammonia emission in all clumps, and N_2H^+ emission in all the 12 sources observed in this line. Only one source has been marginally detected in N_2D^+ (4–3), which is, to our knowledge, the first detection of this line in an IRDC. The clumps have a median mass of $\sim 244 M_\odot$, appear to be gravitationally bound and possess mass, H_2 column and surface densities consistent with being potentially the birthplace of high-mass stars. The most striking result of the work is the high average CO depletion factor (derived from the expected $C^{18}O$ -to- H_2 column density ratio compared to the observed value), which is in between 5 and 78, with a mean value of 32 and a median of 29. These values, derived from the $C^{18}O$ (3–2) transition (which traces gas denser than the lower-excitation lines commonly used in previous works), are larger than the typical CO depletion factors measured towards other IRDCs, and are comparable to or larger than the values derived in the low-mass pre-stellar cores closest to the onset of gravitational collapse. Also, a faint anti-correlation is found between f_D and the gas kinetic temperature. These results suggest that the ear-

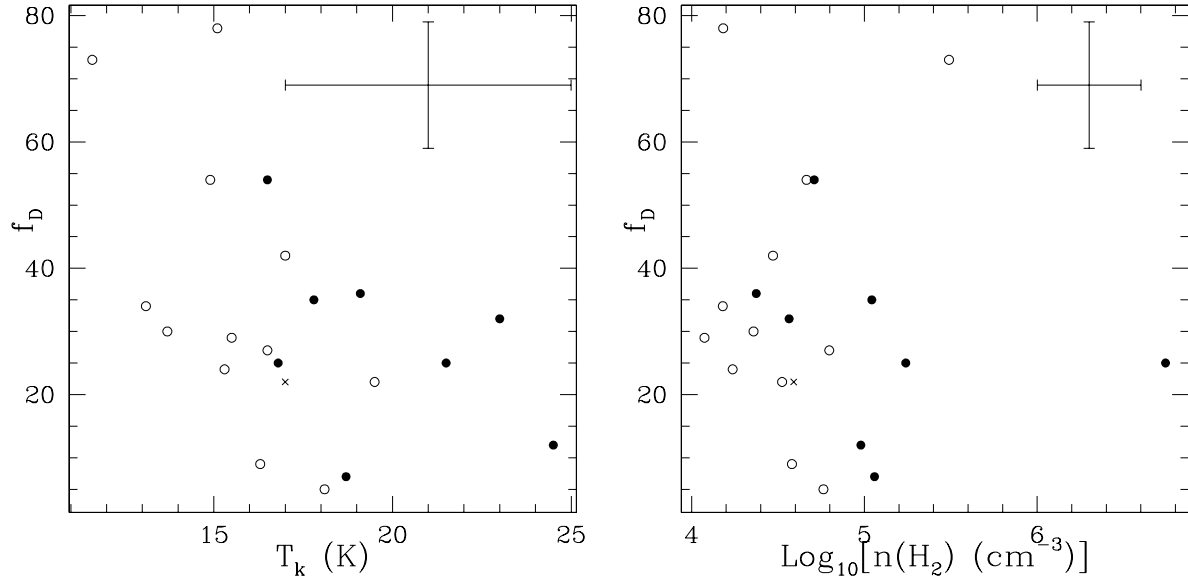


Figure 7. CO depletion factor (f_D) against gas kinetic temperature (left panel) and H₂ volume density (right panel). The symbols have the same meaning as in Fig. 6.

liest phases of the high-mass star and stellar cluster formation process are characterised by CO depletions larger than in low-mass pre-stellar cores. The clumps have an average temperature around 17 K. We have found marginal statistical differences between the clumps detected and undetected in the 24 μm Spitzer images, with the Spitzer-dark clumps being on average colder, less massive and having lower H₂ column and surface densities, but higher CO depletion factors. This indicates that the Spitzer-dark clumps are either less evolved or destined to form stars and stellar clusters less massive than the Spitzer-bright ones.

ACKNOWLEDGMENTS

This publication is based on data acquired with the Atacama Pathfinder Experiment (APEX). The Atacama Pathfinder Experiment is a collaboration between the Max-Planck-Institut für Radioastronomie, the European Southern Observatory, and the Onsala Space Observatory. We thank the staff at the APEX telescope for performing the service mode observations presented in this paper. FF is deeply grateful to Ana López-Sepulcre for providing us with the parameters of the massive cores in López-Sepulcre et al. (2010).

REFERENCES

- Alves, J., Lada, C. J., & Lada, E. A. 1999, *ApJ*, 515, 265
 Battersby, C., Bally, J., Jackson, J. M., et al. 2010, *ApJ*, 721, 222
 Beltrán, M.T., Brand, J., Cesaroni, R., et al. 2006 *A&A*, 447, 221
 Bergin, E.A. & Tafalla, M. 2007, *ARA&A*, 45, 339
 Beuther, H., & Sridharan, T. K. 2007, *ApJ*, 668, 348
 Beuther, H., Schilke, P., Menten, K.M. et al. 2002, *ApJ*, 566, 945
 Brand, J., & Blitz, L. 1993, *A&A*, 275, 67
 Butler, M.J. & Tan, J.C. 2009, *ApJ*, 696, 484
 Busquet, G., Palau, Aina, Estalella, R., et al. 2009, *A&A*, 506, 1183
 Caselli, P. 2011, in "Proceedings of the International Astronomical Union", S280, Vol. 7, pp. 19 - 32
 Caselli, P., Walmsley, C.M., Zucconi, A., et al. 2002a *ApJ*, 565, 344
 Caselli, P., Stantcheva, T., Shalabiea, O., Shematovich, V.I., Herbst, E. 2002b, *P&SS*, 50, 1133
 Chakrabarti, S & McKee, C.F. 2005, *ApJ*, 631, 792
 Chen, H.-R., Liu, S.-Y., Su, Y.-N., Wang, M.-Y. 2011, *arXiv:1110.0952*
 Crapsi, A., Caselli, P., Walmsley, C. M., et al. 2005, *ApJ*, 619, 379
 Emprechtinger, M., Caselli, P., Volgenau, N.H., Stutzki, J., Wiedner, M.C. 2009, *A&A*, 493, 89
 Fontani, F., Palau, A., Caselli, P. et al. 2011, *A&A*, 529, L7
 Fontani, F., Zhang, Q., Caselli, P., Bourke, T.L. 2009, *A&A*, 499, 233
 Fontani, F., Caselli, P., Crapsi, A. et al. 2006, *A&A*, 460, 709
 Fontani, F., Beltrán, M.T., Brand, J. et al. 2005, *A&A*, 432, 921
 Fontani, F., Cesaroni, R., Caselli, P., Olmi, L. 2002, *A&A*, 389, 603
 Foster, J.B., Rosolowsky, E.W., Kauffman, J. et al. 2009, *ApJ*, 696, 298
 Frerking, M., Langer, L., Wilson, R. 1982, *ApJ*, 262, 590
 Fuente, A., Caselli, P., McCoey, C. 2012, *arXiv:1202.5891*
 Hernandez, A.K., Tan, J.C., Caselli, P. et al. 2011, *ApJ*, 738, 11
 Hill, T., Longmore, S.N., Pinte, C. et al. 2010, *MNRAS*, 402, 2682
 Hill, T., Burton, M.G., Minier, V. et al. 2005, *MNRAS*,

- 363, 405
- Ho, P. T. P., & Townes, C. H. 1983, ARA&A, 21, 239
- Jiménez-Serra, I., Caselli, P., Tan, J.C. et al. 2010, MNRAS, 406, 187
- Kauffmann, J. & Pillai, T 2010, ApJ, 273, L7
- Krumholz, M.R., & McKee, C.F. 2008, Nature, 451, 1082
- Lacy, J. H., Knacke, R., Geballe, T. R., & Tokunaga, A. T. 1994, ApJ, 428, L69
- Langer, W. D., Wilson, R. W., Goldsmith, P. F., & Beichman, C. A. 1989, ApJ, 337, 355
- López-Sepulcre, A., Cesaroni, R., Walmsley, C.M. 2010, 517, L66
- MacLaren, I., Richardson, K.M. & Wolfendale, A.W. 1988, ApJ, 333, 821
- Miettinen, O., Hennemann, M., Linz, H 2011, A&A, 534, 134
- Pagani, L., Daniel, F., Dubernet, M.-L. 2009, A&A, 494, 719
- Pillai, T., Kauffmann, J., Wyrowski, F., et al. 2011, A&A, 530, A118
- Pillai, T., Wyrowski, F., Hatchell, J., Gibb, A.G., Thompson, M. A. 2007, A&A, 467, 207
- Pillai, T., Wyrowski, F., Carey, S.J., Menten, K.M. 2006, A&A, 450, 569
- Pineda, J.E., Caselli, P., Goodman, A.A. 2005, ApJ, 679, 481
- Ragan, S.E., Heitsch, F., Bergin, E.A., Wilner, D. 2012, arXiv:1201.1402
- Ragan, S.E., Bergin, E.A., Wilner, D. 2011, arXiv:1105.4182
- Ragan, S.E., Bergin, E.A., Plume, R. et al. 2006, ApJS, 166, 567
- Rathborne, J.M., Simon, R., Jackson, J.M. 2007, ApJ, 662, 1082
- Rathborne, J. M., Jackson, J. M., Zhang, Q., and Simon, R. 2008, ApJ, 689, 1141
- Rathborne, J.M., Jackson, J.M., Chambers, E.T. et al. 2010, ApJ, 715, 310
- Simon, R., Rathborne, J.M., Shah, R.Y. et al. 2006, ApJ, 653, 1325
- Tafalla, M., Santiago-García, J., Myers, P.C. et al. 2006, A&A, 455, 577
- Tafalla, M., Myers, P.C., Caselli, P., & Walmsley, C.M. 2004, A&A, 416, 191
- Vasyunina, T., Linz, H., Henning, Th. et al. 2009, A&A, 499, 149
- Wilson, T.L. & Matteucci, F. 1992, A&AR, 4, 1
- Wilson, T.L. & Rood, R. 1994, ARA&A, 32, 191
- Zhang, Q., Wang, Y., Pillai, T., and Rathborne, J. 2009, ApJ, 696, 268

APPENDIX A: SPITZER AND SIMBA IMAGES

APPENDIX B: SPECTRA

This paper has been typeset from a \LaTeX file prepared by the author.

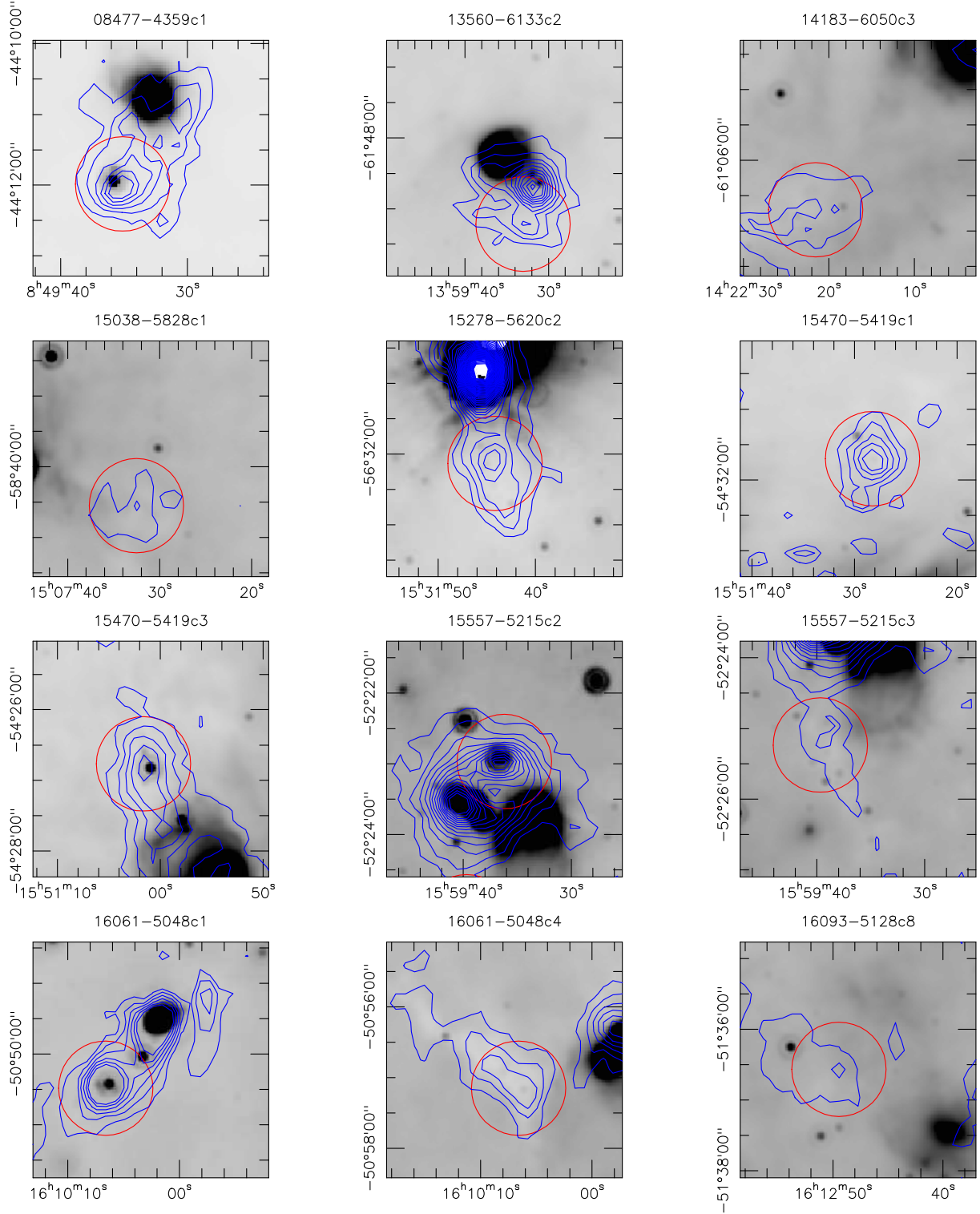


Figure A1. Superimposition of the Spitzer-MIPS 24 μm images on the SIMBA 1.2 mm continuum maps (blue contours: first contour and step correspond to the 3σ rms level) towards the IRDCs studied in this work and observed with Spitzer-MIPS (for clump 13039-6108c6, the Spitzer-MIPS image is not available). In each frame, the red circle indicates the targeted millimetre clump.

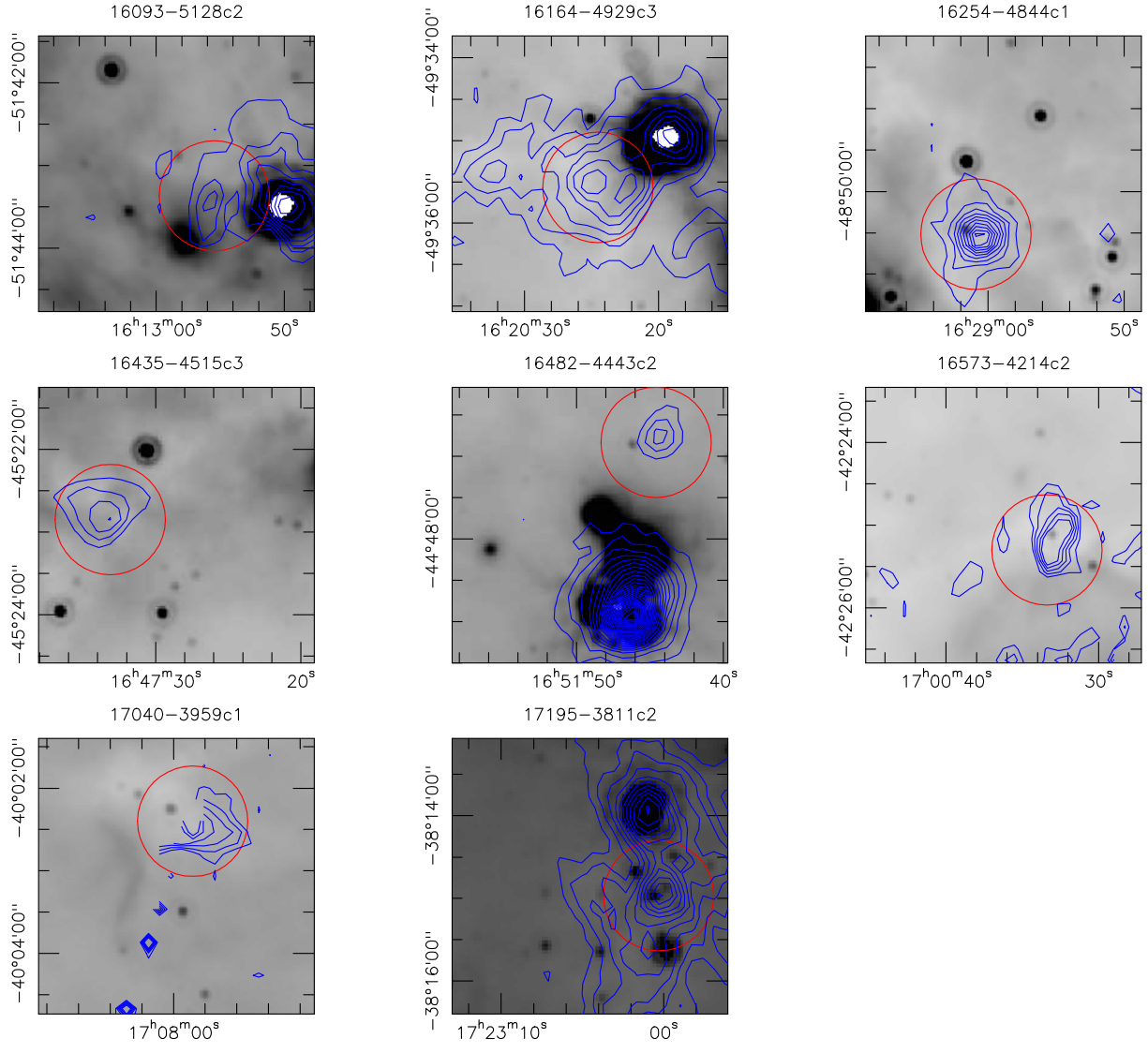


Figure A1. Continued.

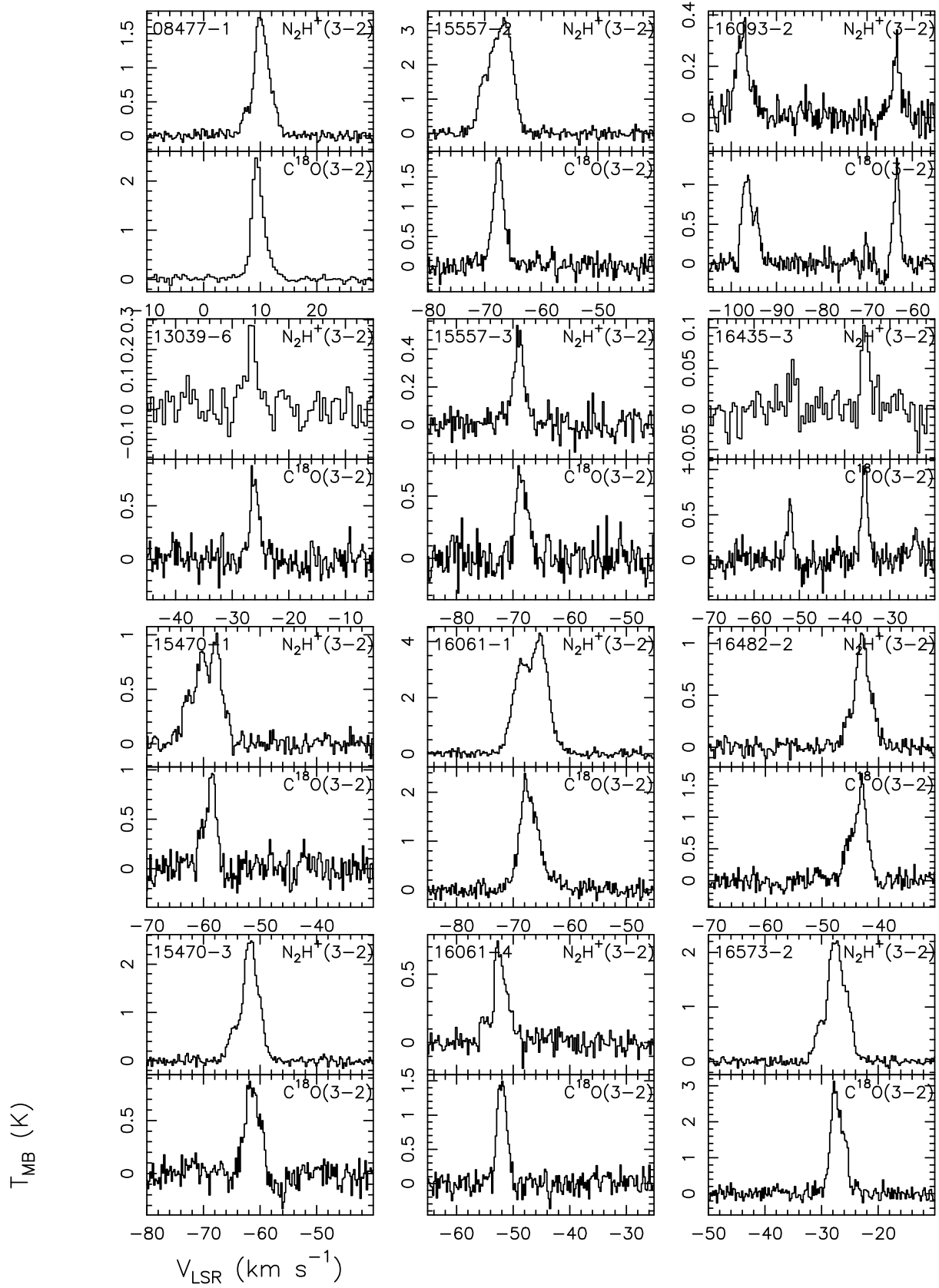


Figure B1. Spectra of the twelve sources observed and detected in both N_2H^+ (3-2) and C^{18}O (3-2). In each frame, we show a range of ± 20 km s $^{-1}$ around the systemic velocity adopted to centre the spectra (given in Table 1) and derived from CS observations. For two objects, 16093-5128c2 and 16435-4515c3, the spectrum contains velocity components separated by several km s $^{-1}$, so that we show a broader velocity range.

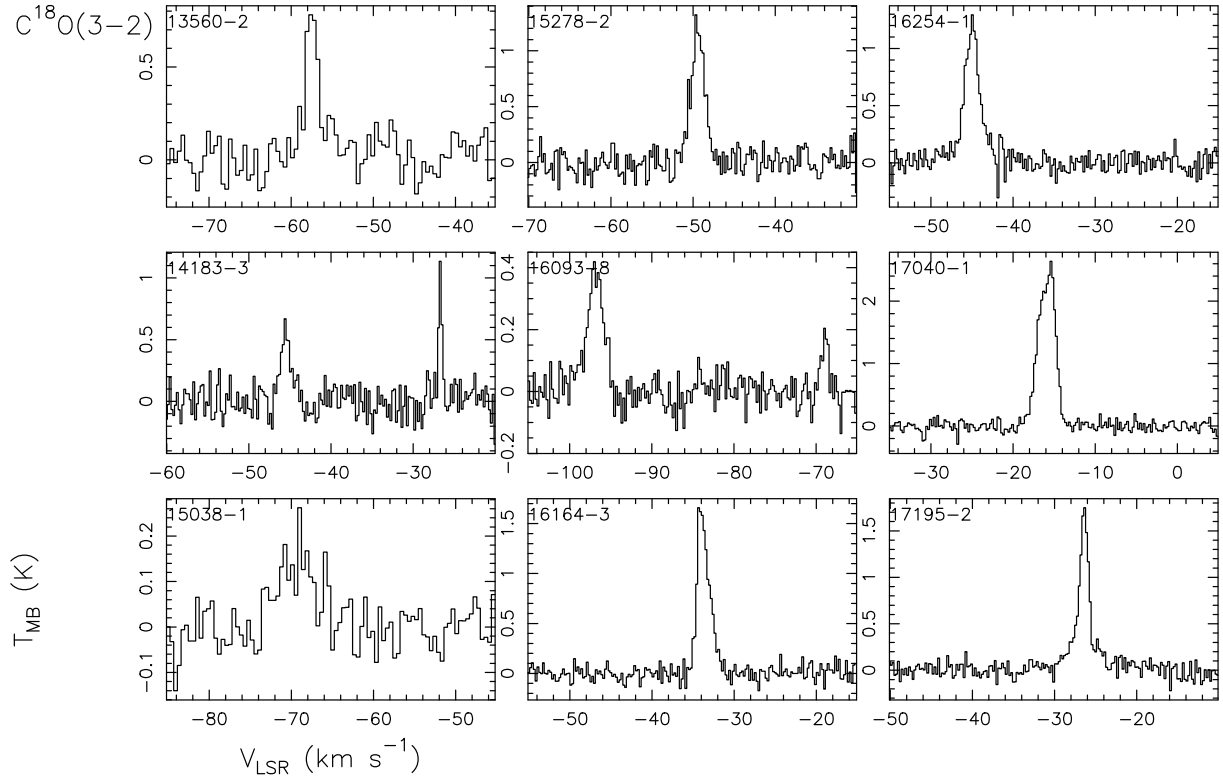


Figure B2. Spectra of the nine sources observed and detected in C^{18}O (3–2) only. As in Fig. B1, the velocity interval on the x-axis range from $V_{\text{LSR}} - 20 \text{ km s}^{-1}$ to $V_{\text{LSR}} + 20 \text{ km s}^{-1}$.